Journal of Geophysics and Engineering, 2026, **23**(1), 197–209
https://doi.org/10.1093/jge/gxaf133
Advance access publication date: 22 October 2025
Research Article

OXFORD

Effects of pressure, fluids, and pore structure on wave attenuation in loading-unloading tests of tight sandstones

Jing Ba[1], Guoqing Jiao[1], Wei Cheng[2,*], José M. Carcione[1,3], Cong Luo[1], Qingchun Jiang[4]

[1]School of Earth Sciences and Engineering, Hohai University, Nanjing 211100, China
[2]SINOPEC Geophysical Research Institute Co., Ltd., Nanjing 211100, China
[3]National Institute of Oceanography and Applied Geophysics (OGS), Trieste, Italy 34010
[4]Department of Geology, Research Institute of Petroleum Exploration and Development, Beijing 100083, China
*Corresponding author. SINOPEC Geophysical Research Institute Co., Ltd., Nanjing, 211100, China. E-mail: chengw.swty@sinopec.com

Abstract

The exploration of petroleum resources is currently extended to unconventional oil/gas reservoirs, such as tight sandstones. These reservoirs require theoretical and experimental studies on the wave response. This study conducts ultrasonic measurements on three tight sandstone samples under varying confining pressures and fluid conditions. To estimate the inverse quality factors of P-waves and S-waves, the spectral ratio theory is employed. With increasing pressure, the P- and S-waves velocities rise, while the attenuation declines. The pressure has the greatest influence on the anelastic properties. At the same pressure, the unloading process exhibits lower attenuation and higher velocities compared with the loading process. This is due to the fact that the cracks do not completely return to their pre-loading state after unloading. A rock-physics model is developed through the Voigt-Reuss-Hill average, the differential effective medium theory, and the squirt-flow model. The model results agree with the experiments. The modeling also shows that with increasing pressure, the attenuation peak in the water-saturated and oil-saturated state gradually shifts to higher frequencies, while the peak in the gas-saturated state shifts to lower frequencies. Water-saturated rocks are less pressure-dependent than oil-saturated rocks, while fully gas-saturated rocks undergo the greatest deformation. This study supports seismic exploration in tight oil and gas reservoirs.

Keywords tight sandstone; wave attenuation; pressure; pore structure; loading; squirt-flow model

1. Introduction

Exploration in the oil and gas industrial sector today takes unconventional resources into account (Zou et al. 2019). In 2020, China produced nearly 70 million tons of oil equivalent from these resources, marking a new phase in the country's oil and gas developments (Zou & Qiu 2021). Oil and gas have been found in tight sandstones, limestones, and other rocks. Notable examples of tight gas include the Xujiahe Formation in southwestern China and the Shanxi and Shihezi Formations in northern China, while tight oil mainly occurs in the Jurassic tight sandstones and limestones in southwestern China and the Mesozoic tight sandstones of the Yanlong Formation in northern China (Zhu et al. 2018). The focus of this study is on tight sandstone formations with strong heterogeneity, developed microcracks, and complex pore structures (Zou et al. 2013). The heterogeneity results from factors such as the arrangement of clay particles, cracks, layering, and low aspect ratio pores (Zhubayev et al. 2016). As micropore structures influence petrophysical attributes and pore fluid distribution, accurately predicting these characteristics is essential for efficient exploration and production. We must provide a crucial theoretical basis for understanding reservoir capacity and revealing oil and gas accumulation patterns.

Seismic wave propagation leads to energy dissipation, which is affected by different mineral proportions, pore and crack structure, confining pressure, and fluid types (Johnston et al. 1979; Ba et al. 2017, 2018; Zhu et al. 2024). Previous research has revealed that pore fluids are an important cause of wave scattering and attenuation (White 1975; Biot 1956, 1962; Bourbié et al. 1987; Sams et al. 1997; Ba et al. 2024). When waves propagate through rock, pressure gradients are generated inside the fluid phase, called wave-induced fluid flow, causing friction between the fluid phase and the solid phase, leading to energy dissipation (Sams et al. 1997; Chapman 2003; Carcione et al. 2010; Müller et al. 2010; Pan et al. 2023; Chen et al. 2023, 2025).

Many experiments have investigated how porosity, permeability, saturation, fluid type, and pressure influence wave attenuation (Dvorkin et al. 1994; Tao et al. 1995; King 2005; Adam et al. 2009; David et al. 2013; Chapman et al. 2016; Ma et al. 2019; Ma & Ba 2020). Gardner et al. (1964) showed that attenuation enhances with saturation and declines with pressure. Winkler & Nur (1979) reported how wave velocity and attenuation are affected by fluid

Received: 23 March 2025. **Revised:** 13 May 2025. **Accepted:** 9 June 2025

saturation, and Toksöz et al. (1979) investigated how fluid and minerals affect P- and S-wave attenuation at ultrasonic frequencies. Johnston & Toksöz (1980) and Oh et al. (2011) found that the attenuation in gas saturation samples is lower than that in water saturation.

Previous studies have established a variety of models to characterize the elastic wave dispersion and attenuation, including models with single and double porosity (Ba 2013; Zhang et al. 2017). Biot (1956) proposed a theory of energy dissipation in homogeneous rock because of the global flow induced by the relative motion of pore fluid and rock matrix. Dvorkin & Nur (1993) combined the global Biot flow and microscopic squirt-flow theories to obtain a unified model, referred to as the BISQ model. Berryman & Milton (1991) extended the Gassmann equation to materials containing two different pore systems. Given the complex pore structures and significant heterogeneity of tight sandstone deposits, additional research on wave attenuation in these rocks is warranted.

This study presents ultrasonic investigations of tight sandstone samples. To obtain the attenuation of P- and S-waves, we use the spectral ratio method. A model is formulated using the squirt-flow model, Voigt-Reuss-Hill (VRH) average, and differential effective medium (DEM) theory. The influence of fluid types, loading and unloading on the P-waves and S-waves velocities, attenuation and pore structure are studied, which provides valuable insights for exploration practice in tight reservoirs.

2. Experiments

2.1. Samples

The Sichuan Basin is a large superimposed petroliferous basin and serves as a crucial base for China's oil and gas industry. Among the discovered hydrocarbon-bearing formations, the continental Jurassic system hosts the shallowest reservoirs. The Jurassic Shaximiao Formation is one of the key productive strata. The Longmenshan frontal structural belt is located in the western Sichuan Basin, between the two thrust faults—the Guankou Fault and the Pengxian Fault. It is bounded by the Longmenshan frontal fault zone to the west and adjoins the Chengdu Depression and the Xinchang structural belt to the east. The tight sandstone samples originate from the gas reservoirs of the Shaximiao Formation in this region. The Shaximiao Formation is a near-source sedimentary sequence with a thickness of 700–800 m, consisting of interbedded sandstone and mudstone layers. The sandstone reservoirs exhibit considerable lateral variations, strong heterogeneity, and a complex pore structure with a weak impedance contrast to the surrounding rocks. The reservoirs exhibit a shallow water delta front depositional system with multiple submarine distributary channels. It is described as low porosity, low permeability, and thin layers. These rock types include feldspathic and feldspar-lithic sandstones.

Three samples are prepared as cylindrical specimens (50 mm in length, 25 mm in diameter). Table 1 lists the properties of the samples, with mineral composition identified by a thin-section analysis. The samples have low porosity and permeability, less than 15% and 1 mD, respectively. The thin slice images of three samples are shown in Fig. 1, with quartz being the predominant mineral, followed by feldspar and lithic fragments. The cementing materials consist mainly of clay and calcite. Sample TS2 has relatively larger mineral grains, with more pronounced sericitization and clay on the feldspar surfaces. We measure the porosities and permeabilities of the samples by using the automatic permeameter

Table 1 Properties of tight sandstone samples.

Samples	TS1	TS2	TS3
Dry-rock density (kg/m^3)	2440	2350	2590
Porosity (%)	8.53	11.27	3.30
Permeability (mD)	0.1490	0.3985	0.0445
Feldspar (%)	22	22	22
Quartz (%)	61	61	64
Lithic (%)	17	17	14

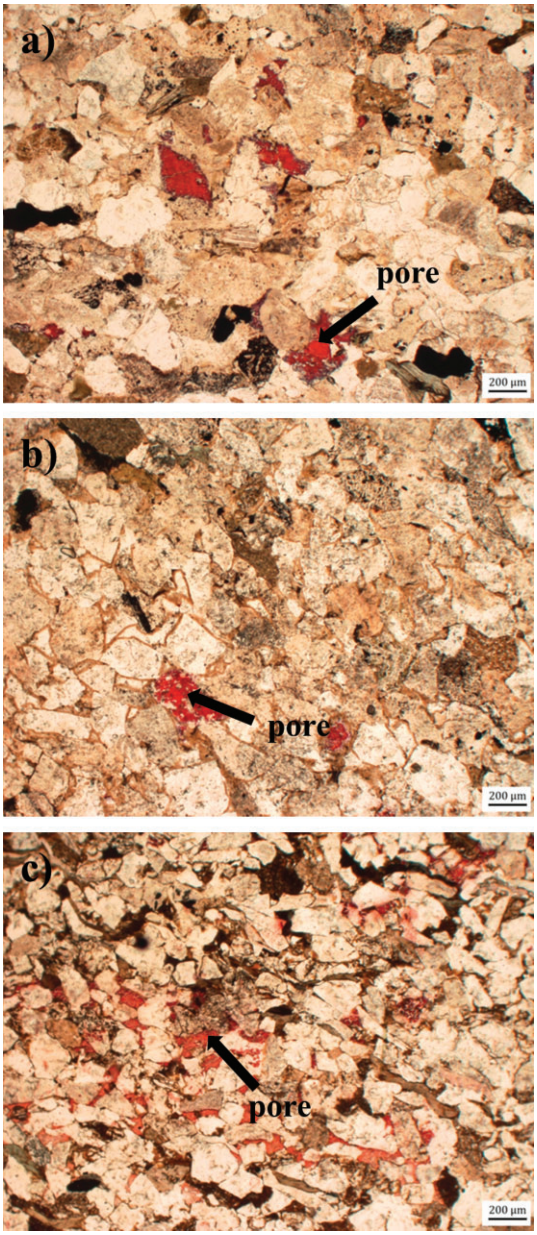

Figure 1 Thin section images. (a) TS1, (b) TS2, (c) TS3.

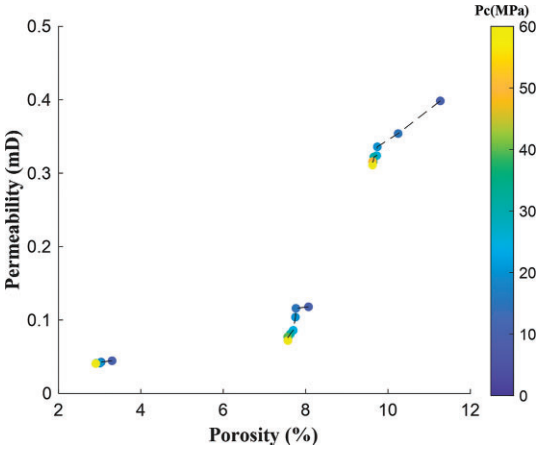

Figure 2 Porosity and permeability under varying confining pressures.

Table 2 Physical properties of pore fluid.

	Nitrogen	Brine	Kerosene
Density (kg/m^3)	129	1003	758
Viscosity (cP)	0.0181	0.892	7.86
Bulk moduli (GPa)	0.0278	2.252	1.342

of the core measurement system. Figure 2 gives the porosity and permeability results at different confining pressures, showing that the porosity and permeability decrease with increasing pressure. The trend is primarily attributed to the closure of pores/cracks under pressure conditions.

2.2. Ultrasonic tests

This study considers the effects of three fluid types on the tight sandstone samples: nitrogen, brine, and kerosene. The specific fluid parameters are provided in Table 2. The gas(nitrogen)-saturated samples are placed in a core ultrasonic meter. A confining pressure of between 12 and 60 MPa is applied, including nine pressure points of 12, 15, 20, 25, 30, 35, 40, 50, and 60 MPa. After each loading, the samples are stabilized for a certain time to ensure pore pressure equilibrium. The stabilization time is influenced by the permeability and the fluid viscosity (samples with lower permeability and higher fluid viscosity require longer stabilization time). The frequency of the generated pulse is approximately 500 KHz.

During saturation with oil or brine, the samples are saturated under vacuum pressure due to their low porosity and permeability. The samples are deposited in a vacuum chamber saturated with kerosene or 5% NaCl solution until no more bubbles are visible on the sample surface. The sample is considered completely saturated when no further change in mass is detected on repeated weighing and when the product of pore volume and fluid density matches the increase in mass. After saturation, the samples are loaded into the ultrasonic measuring device. Then we pump the corresponding fluid to maintain pore pressure. The further procedures are the same as for the experiments with gas-saturated samples.

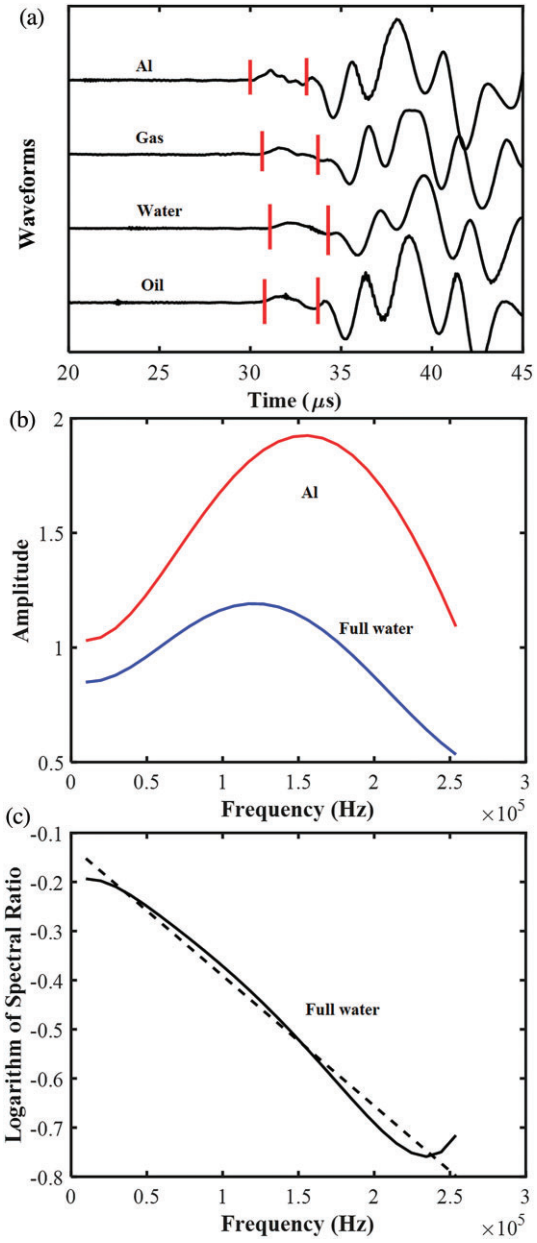

Figure 3 Estimation of the S-waves attenuation for sample TS3. (a) Selection of time windows for aluminum, gas-, water- and oil-saturated samples; (b) Fourier transform to obtain the spectra; (c) estimation of Q with a logarithmic least squares fitting based on the spectral ratio.

2.3. Estimation of the wave attenuation

This article uses the spectral ratio theory to calculate the attenuation of P- and S-waves (Toksöz et al. 1979; Quan & Harris 1997; Zhang & Ulrych 2002; Picotti & Carcione 2006). The plane wave amplitudes of the rock and aluminum sample are

$$A_1(f) = G_1(x)\mathrm{e}^{-\alpha_1(f)x}\mathrm{e}^{-i(2\pi ft - m_1 x)}, \quad (1a)$$

$$A_2(f) = G_2(x)\mathrm{e}^{-\alpha_2(f)x}\mathrm{e}^{-i(2\pi ft - m_2 x)}, \quad (1b)$$

where the subscripts 1 and 2 refer to rock sample and aluminum, respectively, x is the distance, f is the frequency, t is the propaga-

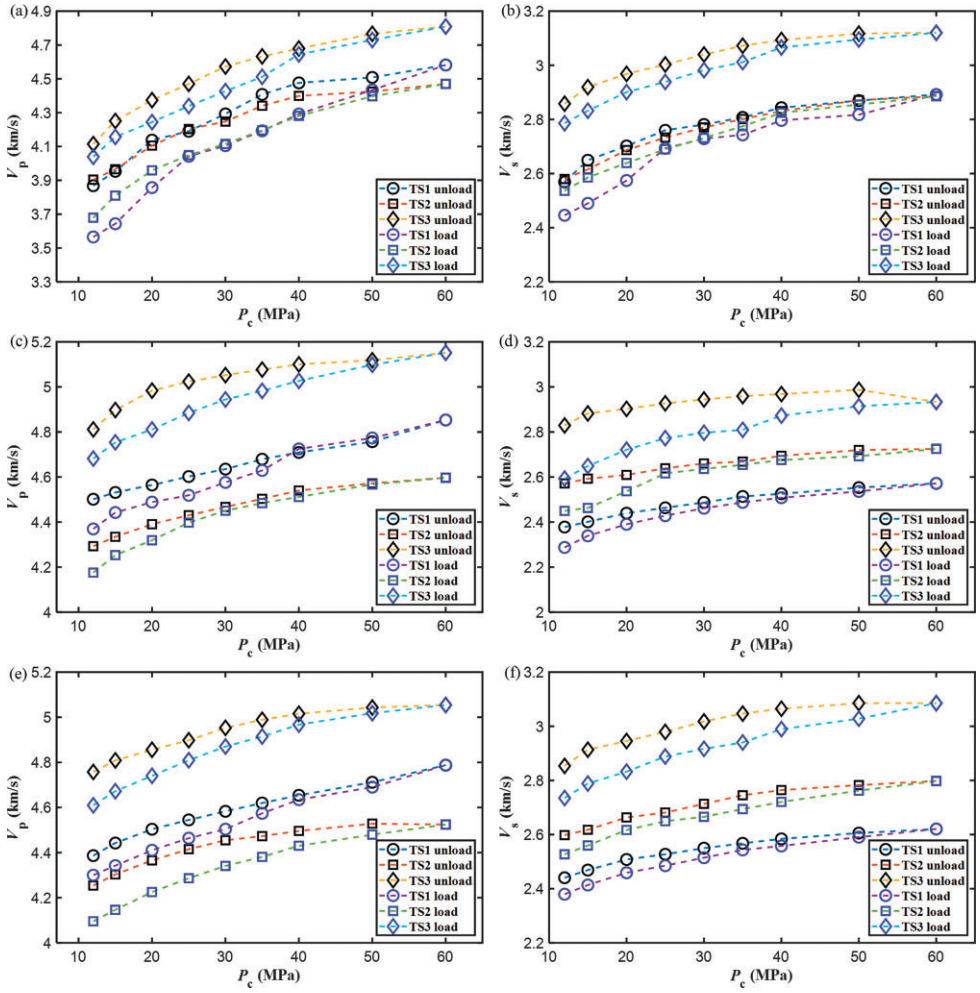

Figure 4 Effects of loading (blue symbols) and unloading (black symbols) on the velocities. (a), (c), and (e) indicate the P-waves velocities under gas-, water- and oil-saturated conditions, respectively; (b), (d), and (f) show the corresponding S-waves velocities.

tion time, m_1, m_2 are wave numbers, and $G_1(x)$, $G_2(x)$ are geometric factors independent of frequency. The attenuation factors are

$$\alpha_1 = \frac{\pi f}{Q_1 V_1}, \quad \alpha_2 = \frac{\pi f}{Q_2 V_2}, \tag{2}$$

where f is frequency, Q_1 and Q_2 are the quality factors, and V_1, V_2 are the wave velocities.

Since the quality factor of rock is much lower than that of aluminum, α_2 can be assumed to be zero. Therefore,

$$\ln\left(\frac{A_1(f)}{A_2(f)}\right) = -\frac{\pi x}{Q_1 V_1} f + \ln\frac{G_1(x)}{G_2(x)}. \tag{3}$$

Figure 3 shows the estimation process of S-wave attenuation for one of the samples. The waveforms of the reference material and sample with different fluid types are given and several periods are selected as time windows (Fig. 3a). A Fourier transform is applied to obtain the spectrum at full water saturation (Fig. 3b), calculate the spectrum ratio curve, perform a linear fit in the main frequency band (Fig. 3c), and obtain the quality factor Q.

3. Experimental results

The effect of loading and unloading processes on the P-wave and S-wave velocities is displayed in Fig. 4. When the confining pressure increases, both velocities increase, with a greater increase observed at low pressures. This indicates that, at low pressures, the closing (or opening) of cracks is more pronounced. At higher pressures, the cracks exhibit a tendency to close and the rate of velocity growth decreases. At the same confining pressure, the velocities are higher under the unloading conditions, which is due to the inelastic deformation during loading, as the cracks are closed during loading and are unlikely to fully reopen during unloading.

In addition, at the same conditions, the P-waves velocity is highest under water saturation. For S-waves, the velocity exhibits maximum value in the gas saturation state, followed by the oil and water states. This illustrates how the type of fluid affects the propagation of elastic waves, with significant effects on the velocities.

Figure 5 illustrates the influence of loading and unloading on the attenuation. When confining pressures elevate, wave attenuation exhibits a reduction due to crack closure and the restriction of fluid motion between fractures and intergranular spaces. Under

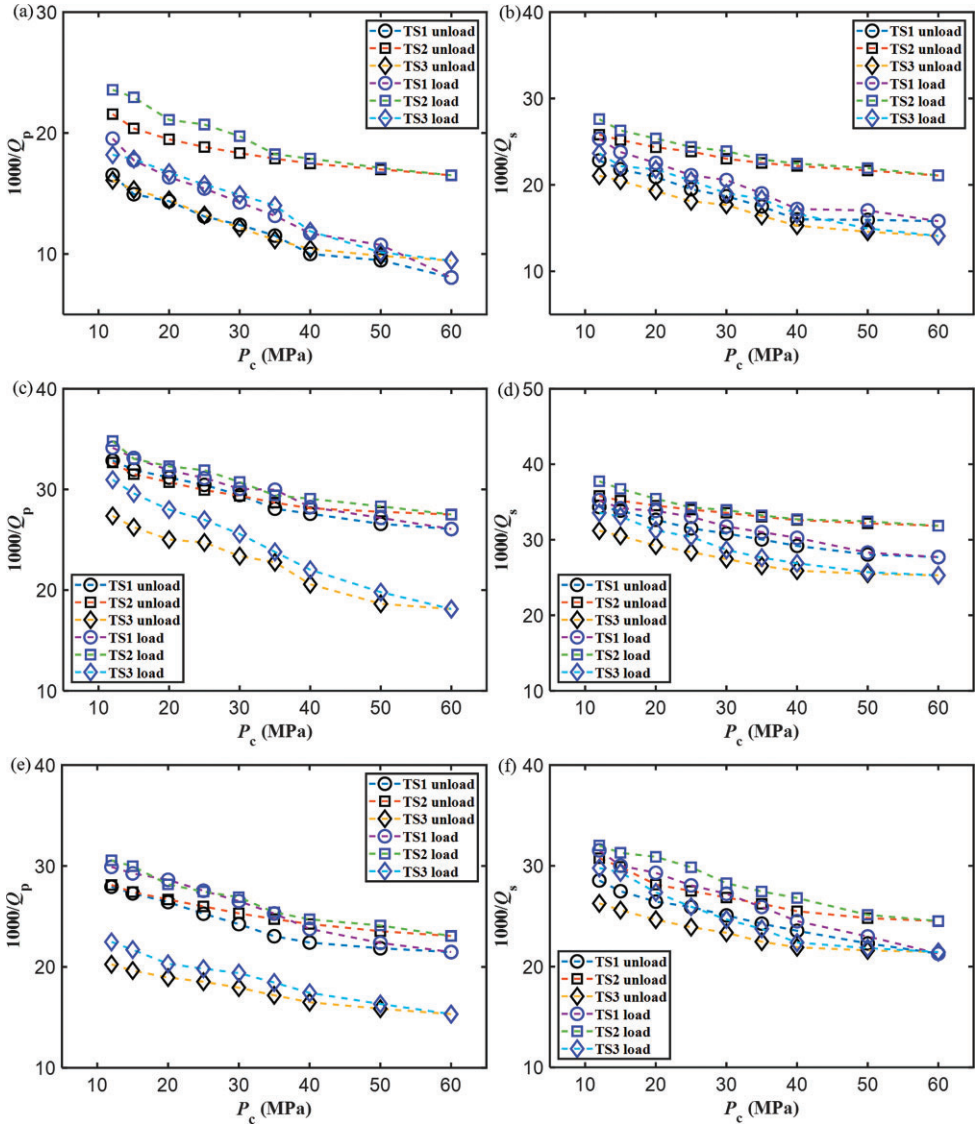

Figure 5 Effects of loading (blue symbols) and unloading (black symbols) on the attenuation. (a), (c), and (e) indicate the P-waves attenuation under gas-, water- and oil-saturated conditions, respectively; (b), (d), and (f) show the corresponding S-waves attenuations.

the same confining pressures, attenuation is highest in the water-saturated state, followed by the oil case. This trend is due to the viscoelastic behavior of solid-fluid interactions during wave transmission (Wang et al. 2006). Compared with the gas-saturated state, water saturation increases the anelasticity of the rock, resulting in greater viscous absorption of the elastic waves and higher attenuation.

The velocity–attenuation relationships for the three samples are shown in Fig. 6. When the confining pressures elevate, the velocities increase while the attenuation decreases.

4. Squirt-flow model

4.1. Modeling process and methods

A suitable model is required for interpreting the experiment results regarding the impact of confining pressure and pore fluids on P- and S-wave propagation. Figure 7 illustrates the modeling process. First, the dry-rock moduli are calculated by using the VRH average and the differential effective medium model (Reuss 1929; Hill 1952). A squirt-flow model is applied for fluid substitution to analyze wave responses under varying confining pressures and saturating fluids.

4.1.1. P- and S-waves velocities and attenuation

Gurevich et al. (2010) presented a model for porous media, which has stiff and soft pores. At low-frequency limit, the model adopts the Gassmann equation (Gassmann 1951). At high-frequency limit, it approaches the Mavko-Jizba equation (Mavko & Jizba 1991). The assumption of this model is that soft pore is saturated and stiff pore is not. Within a single wave cycle, the pore fluid pressure gradient is not equilibrated at high frequencies, resulting in a non-relaxed state.

The modified frame bulk and shear moduli are determined with

$$\frac{1}{K_{mf}} = \frac{1}{K_h} + \frac{1}{\frac{1}{1/K_d(P_c)-1/K_h} + \frac{1}{\phi_s(1/K_f^*-1/K_g)}}, \tag{4a}$$

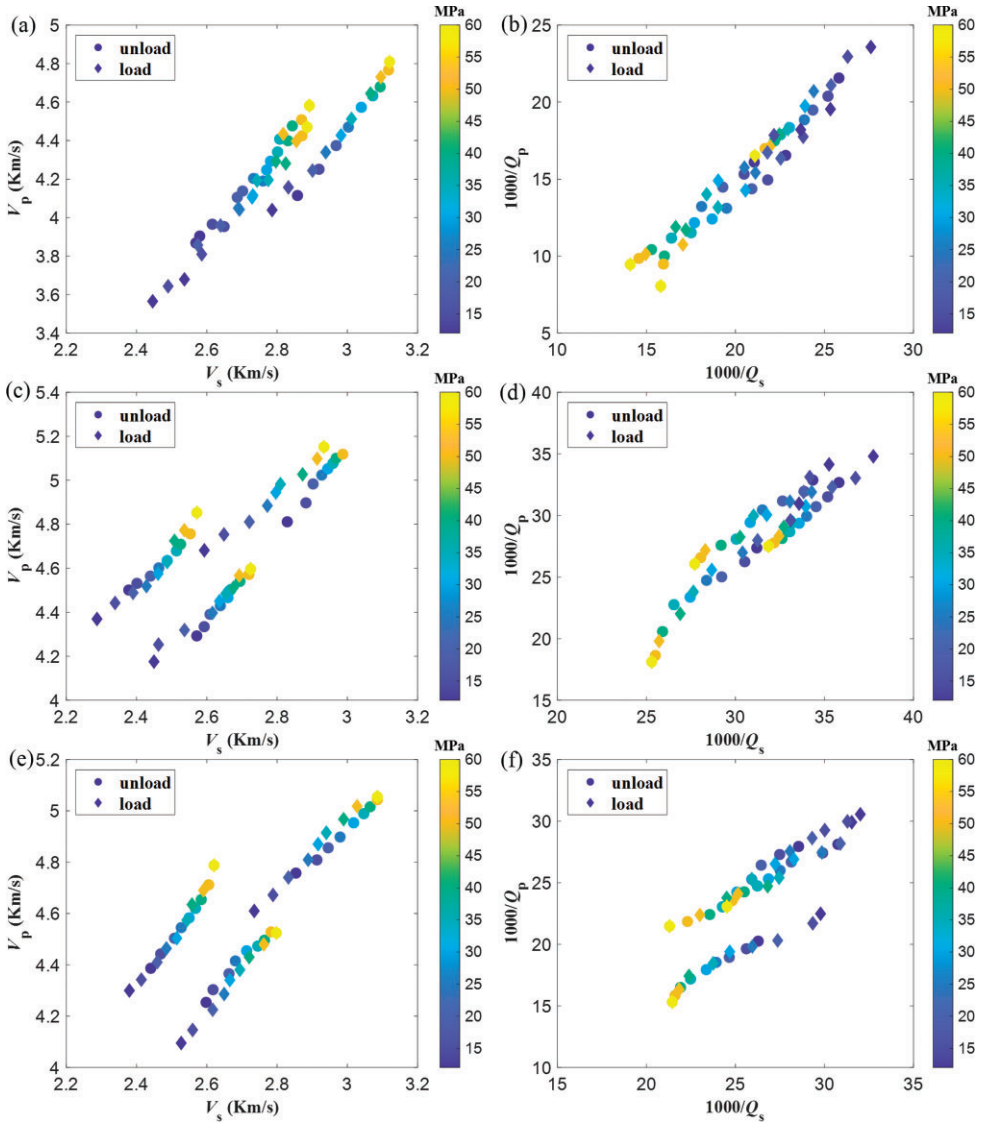

Figure 6 Cross-plots of P-wave velocities and attenuation (1000/Q_P) at full saturation. (a) and (b) show the gas-saturated case; (c) and (d) show the water-saturated case; (e) and (f) show the oil-saturated case.

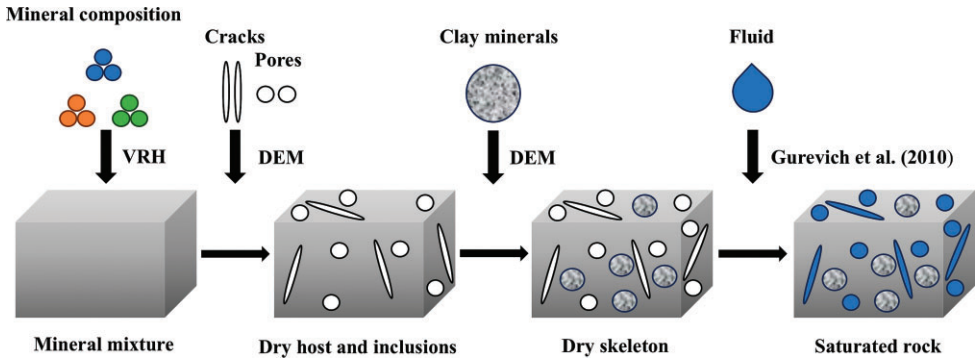

Figure 7 Modeling chart to incorporate the squirt-flow effects.

$$\frac{1}{\mu_{mf}} = \frac{1}{\mu_d(P_c)} - \frac{4}{15}\left(\frac{1}{K_d(P_c)} - \frac{1}{K_{mf}}\right), \tag{4b}$$

where $K_d(P_c)$ and $\mu_d(P_c)$ are the respective moduli of the dry frame, K_h is the bulk modulus of the dry rock with soft pores closed, K_g is the bulk modulus of the mineral mixture, and ϕ_s is the soft (crack) porosity (Carcione 2022, section 7.15; Berryman 2007; Gurevich et al. 2010; Pan et al. 2023).

The complex fluid bulk modulus can be represented through the following equation as

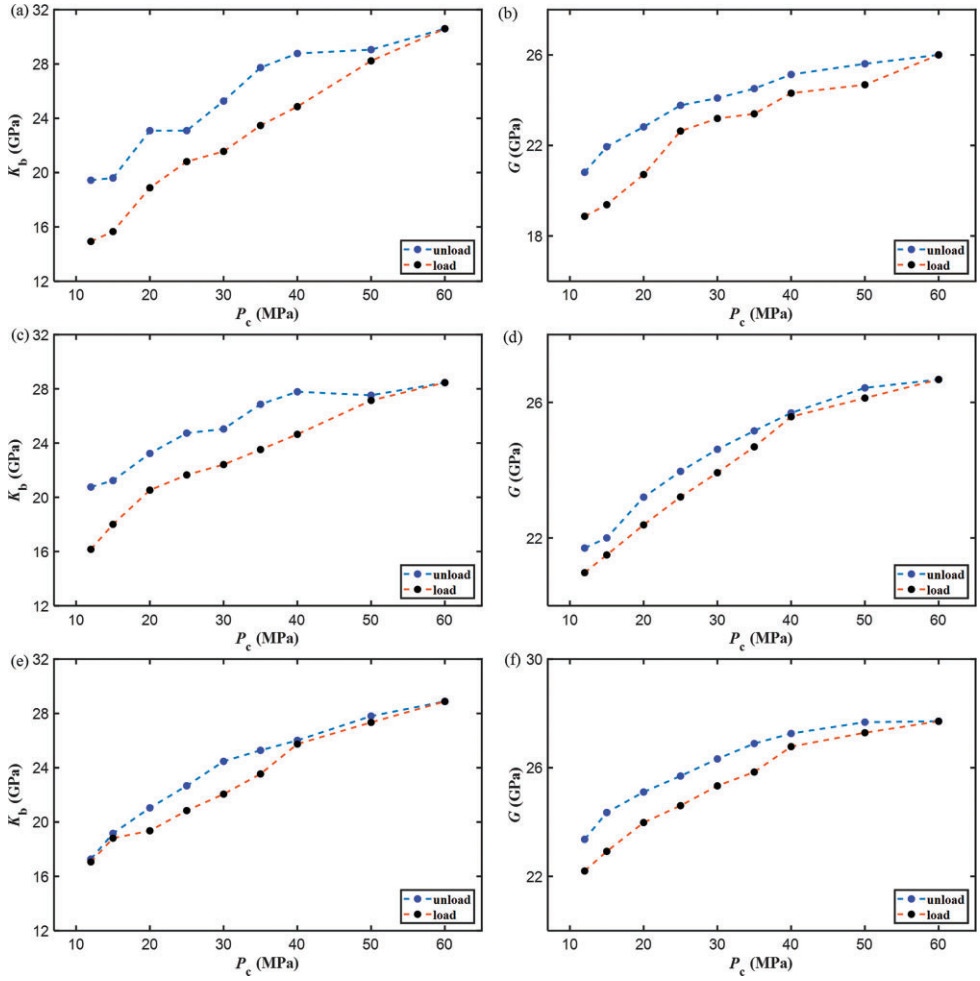

Figure 8 Dry rock bulk and shear moduli. (a) and (b) represent sample TS1; (c) and (d) represent TS2; (e) and (f) represent TS3.

$$K_f^* = \left(1 - \frac{2J_1(ka)}{kaJ_0(ka)}\right) K_f, \tag{5}$$

where K_f is the bulk moduli of fluid, J_0 is the first-order Bessel functions, J_1 is the second-order Bessel functions. ka can be obtained by

$$ka = \frac{1}{\alpha}\left(-\frac{3i\omega\eta}{K_f}\right)^{1/2}, \tag{6}$$

where α is the aspect ratio of soft pore, ω is the angular frequency, η is the viscosity of fluid.

The bulk and shear modulus are

$$\mu_{sat} = \mu_{mf}, K_{sat} = K_{mf}. \tag{7}$$

The dissipation of P-waves and S-waves is

$$Q_p^{-1} = \frac{\mathrm{Im}(V_p^2)}{\mathrm{Re}(V_p^2)}, \quad Q_s^{-1} = \frac{\mathrm{Im}(V_s^2)}{\mathrm{Re}(V_s^2)}, \tag{8}$$

where the P-waves and S-waves complex velocities are

$$V_p = \sqrt{\frac{K_{sat}}{\rho} + \frac{4}{3}V_s^2}, \quad V_s = \sqrt{\frac{\mu_{sat}}{\rho}}. \tag{9}$$

The phase velocities can be expressed (Carcione 2022) as

$$\overline{V_p} = \left[\mathrm{Re}\left(\frac{1}{V_p}\right)\right]^{-1}, \quad \overline{V_s} = \left[\mathrm{Re}\left(\frac{1}{V_s}\right)\right]^{-1}. \tag{10}$$

The bulk density can be expressed as

$$\rho = \rho_d(1 - \phi(P_c)) + \phi(P_c)\rho_f, \tag{11}$$

where ρ_d is the density of dry rocks, ρ_f is the density of fluid, and $\phi(P_c)$ is the total porosity.

4.2. Wave response

By using the equation of Batzle and Wang to calculate the properties of fluid (Batzle & Wang 1992), Table 2 gives the properties of pore fluid (nitrogen, brine, and kerosene) at 30°C and pore pressure of 10 MPa.

The mineral compositions are identified with the single- and orthogonal-polarized thin sections. The minerals are mainly quartz, including feldspar and lithic fragments. The pore-filling materials are mainly clay and calcite. The predominant pore types are intergranular (stiff or equant pores) and microfractures (cracks or soft pores). The VRH average is applied to obtain grain's bulk modulus. Furthermore, the DEM model is utilized to estimate the dry rock moduli. Figure 8 indicates that as confining pressure

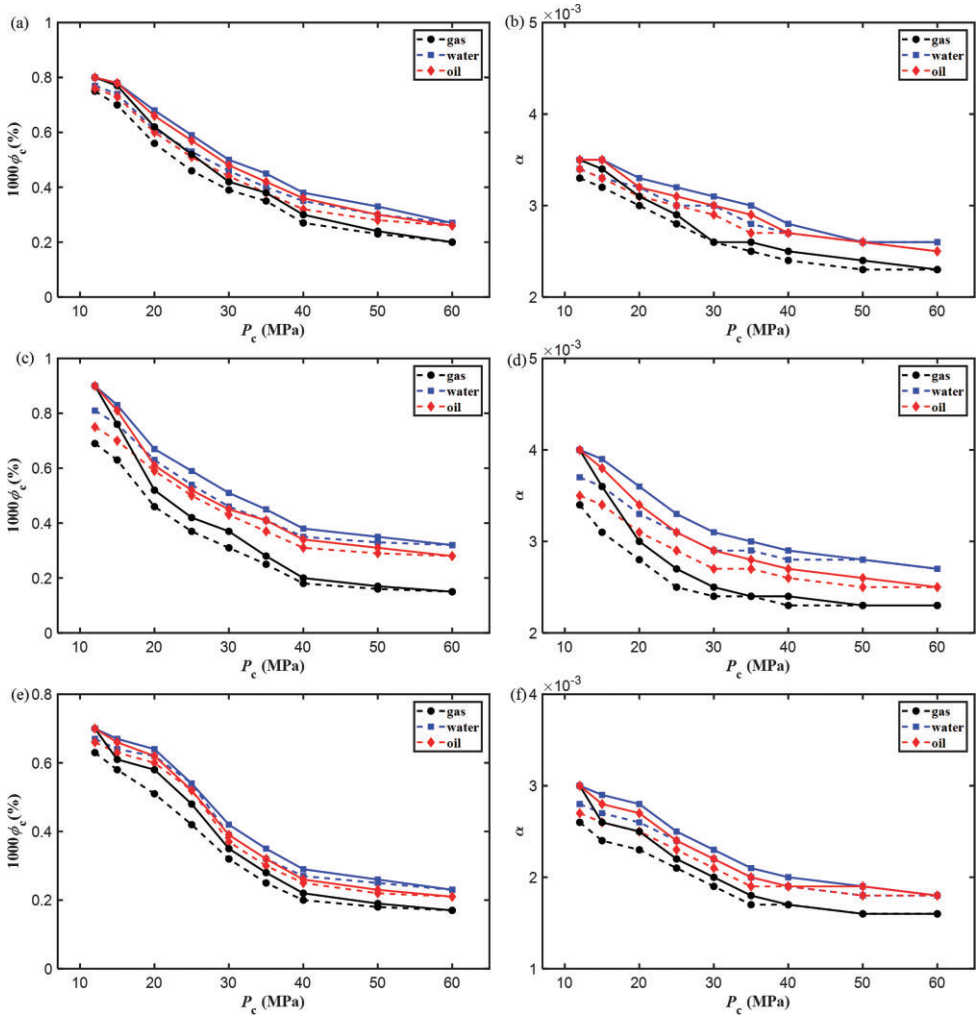

Figure 9 Soft porosity and aspect ratio vary with confining pressure. (a) and (b) represent TS1; (c) and (d) represent TS2; (e) and (f) represent TS3. The solid and dashed lines represent loading and unloading conditions, respectively.

increases both moduli increase. The trends under loading and unloading conditions are similar, with higher values at unloading conditions. Based on the experiments, the relationship between attenuation and frequency as a function of confining pressure is obtained by using Equations (4 to 11).

According to the data of Table 2 and Fig. 8, the model parameters are given, including fluid density, viscosity, and bulk modulus, as well as the bulk and shear modulus of dry rocks. By utilizing Equations (4 to 11), the velocities and attenuation are modeled. When the simulated results generally align with the experimental data, the soft-pore porosity and crack aspect ratio parameters are obtained through modeling. The soft porosity and aspect ratio (obtained with modeling) is shown in Fig. 9. The stiff and soft porosities are difficult to measure experimentally, but can be calculated with empirical equations. In this study, Han et al.'s (2018) method is used, with the pore aspect ratio treated as a fitting parameter (Han et al. 2018). The initial soft porosities for samples TS1, TS2, and TS3 are 0.0008, 0.0009, and 0.0007, respectively, and the corresponding aspect ratios are 0.0035, 0.004, and 0.003. At low confining pressures, a significant decrease in both properties is observed, which depends on the saturating fluid, with lower values for gas. The differences between the water and oil cases are less pronounced, with higher values for water.

After unloading, both properties are lower than their original values, indicating that non-elastic deformation has occurred and the cracks have not been fully recovered. Water-saturated specimens show higher values, indicating that the deformation after compression is influenced by the nature of the fluid.

The variation pattern under oil-saturated conditions is consistent with the under-water-saturated condition. The example is given for the water-saturated case in this study. Figures 10 and 11 indicate the theoretical P-wave and S-wave attenuation of three tight sandstone samples under gas and water saturations during loading contrasted with the experimental data. The two sets of data show good agreement. Furthermore, for all fluid types, the peak P- and S-waves attenuation decreases with rising pressure as a result of the closure of soft pores, which limits the local pore fluid flow. In addition, with increasing pressure, the attenuation peaks will shift to higher frequencies for water and oil saturations, whereas for gas saturation, the peak shifts to lower frequencies.

The same results for unloading are shown in Fig. 12 and Fig. 13. The peak attenuation values are slightly lower than for those in loading, with the S-waves showing a clearer difference. The model predictions basically fit well with the experimental data. For sample TS3 under gas-saturated conditions, a slight discrepancy is

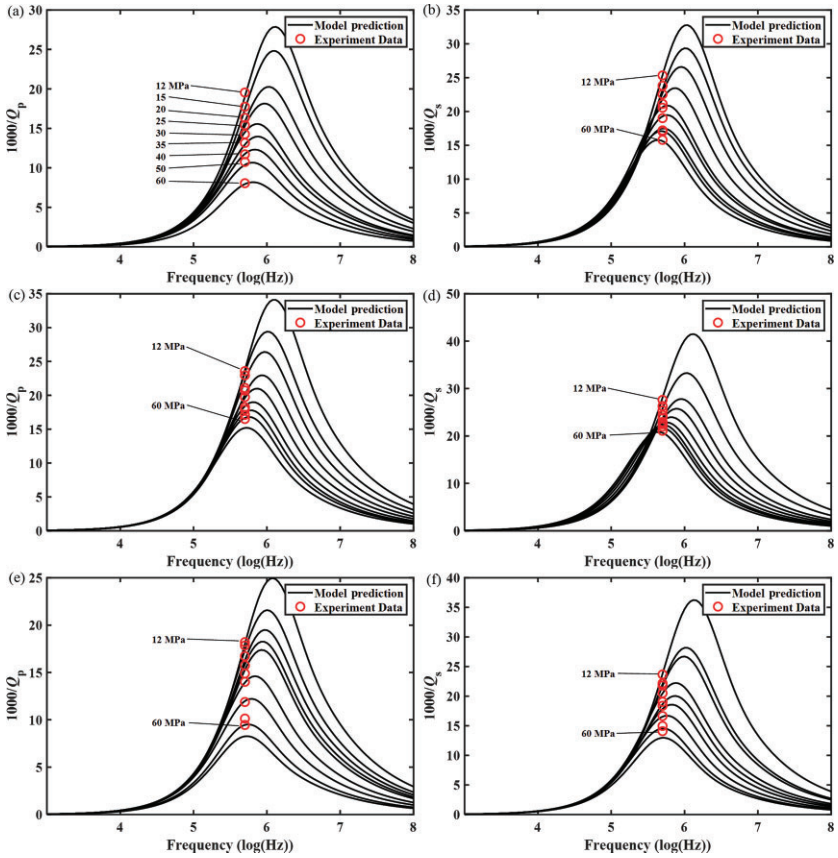

Figure 10 P-waves and S-waves attenuation at the gas-saturated case under loading conditions. (a) and (b) represent the sample TS1; (c) and (d) represent TS2; (e) and (f) represent TS3. The red circles represent experimental data.

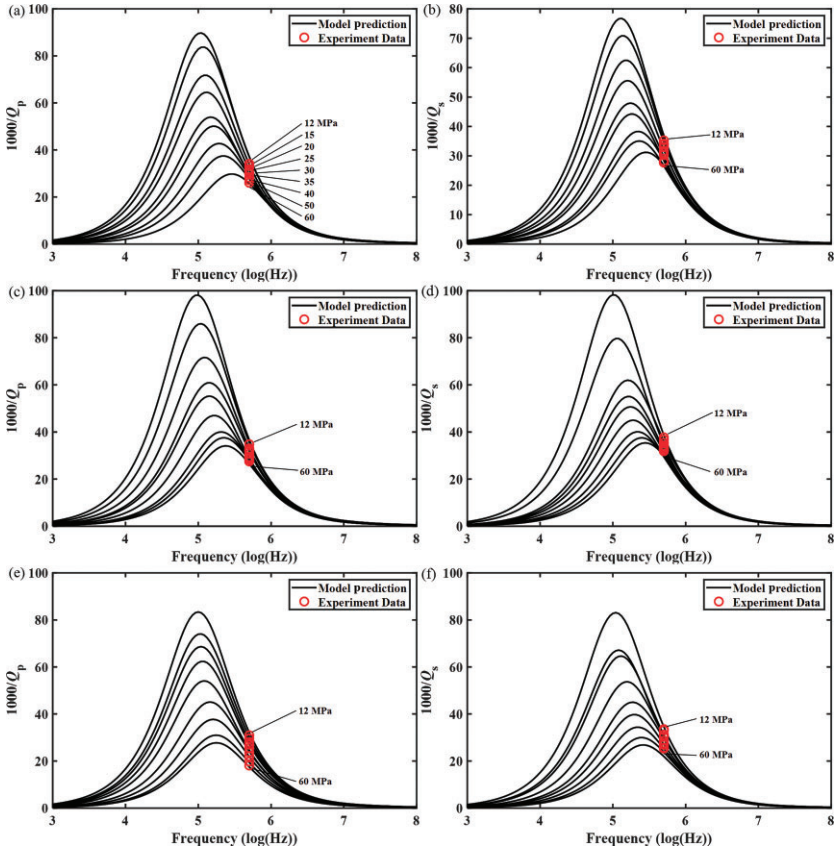

Figure 11 P-waves and S-waves attenuation at the water-saturated case under loading conditions. (a) and (b) represent the sample TS1; (c) and (d) represent TS2; (e) and (f) represent TS3. The red circles represent experimental data.

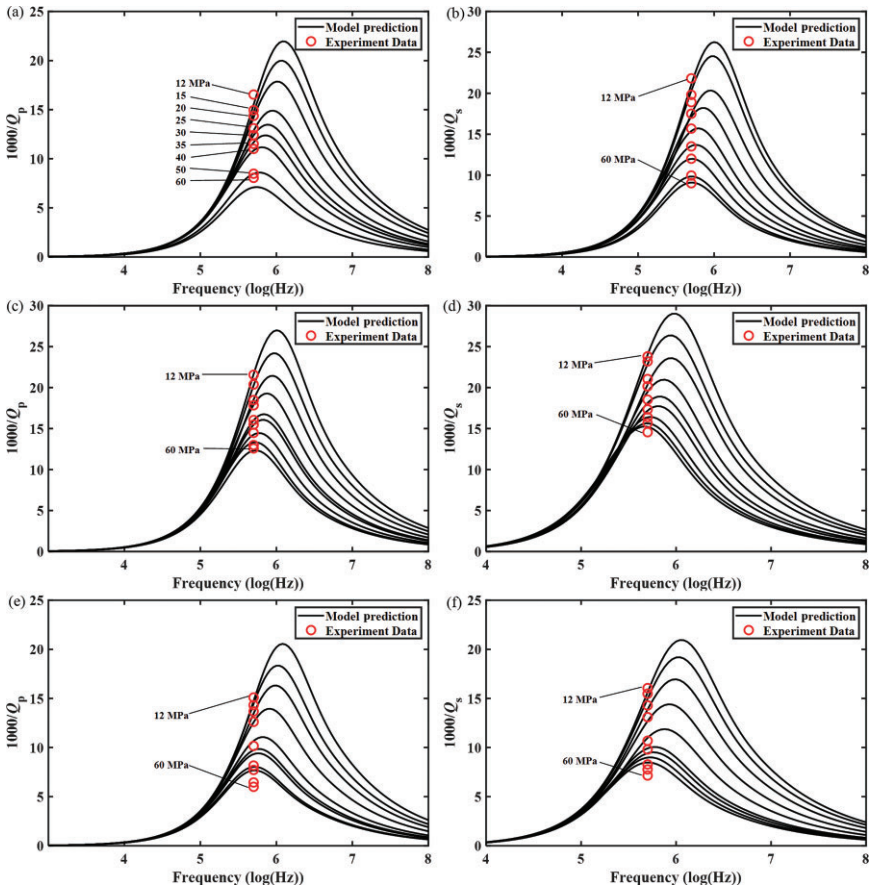

Figure 12 Same as Fig. 10 for unloading conditions.

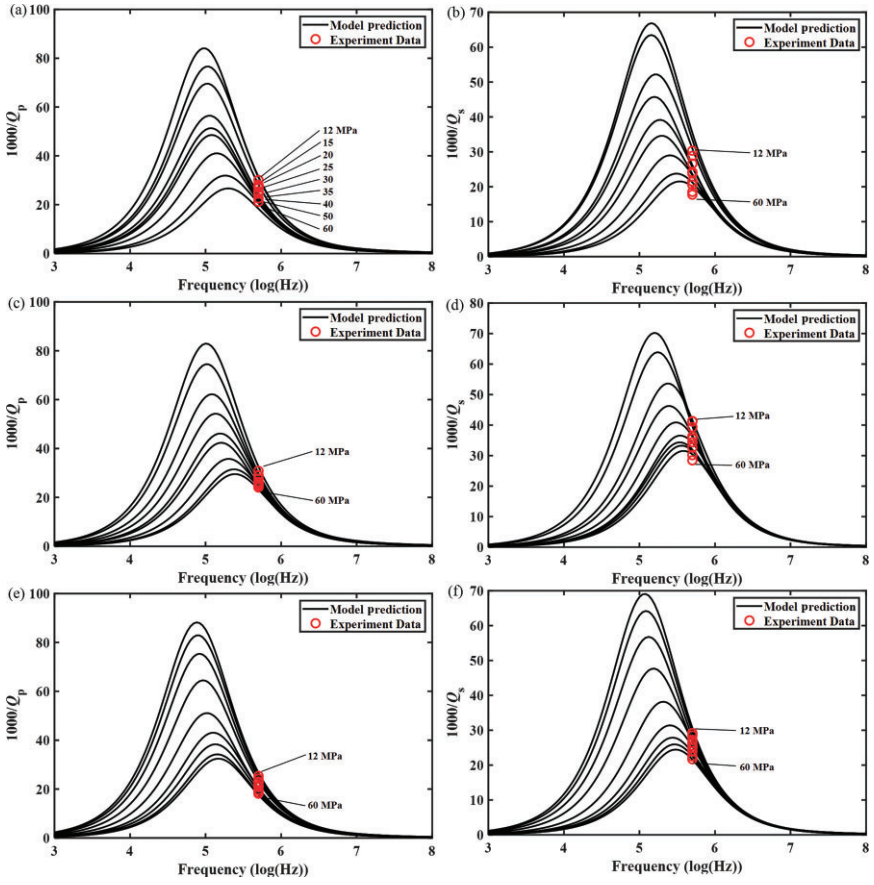

Figure 13 Same as Fig. 11 for unloading conditions.

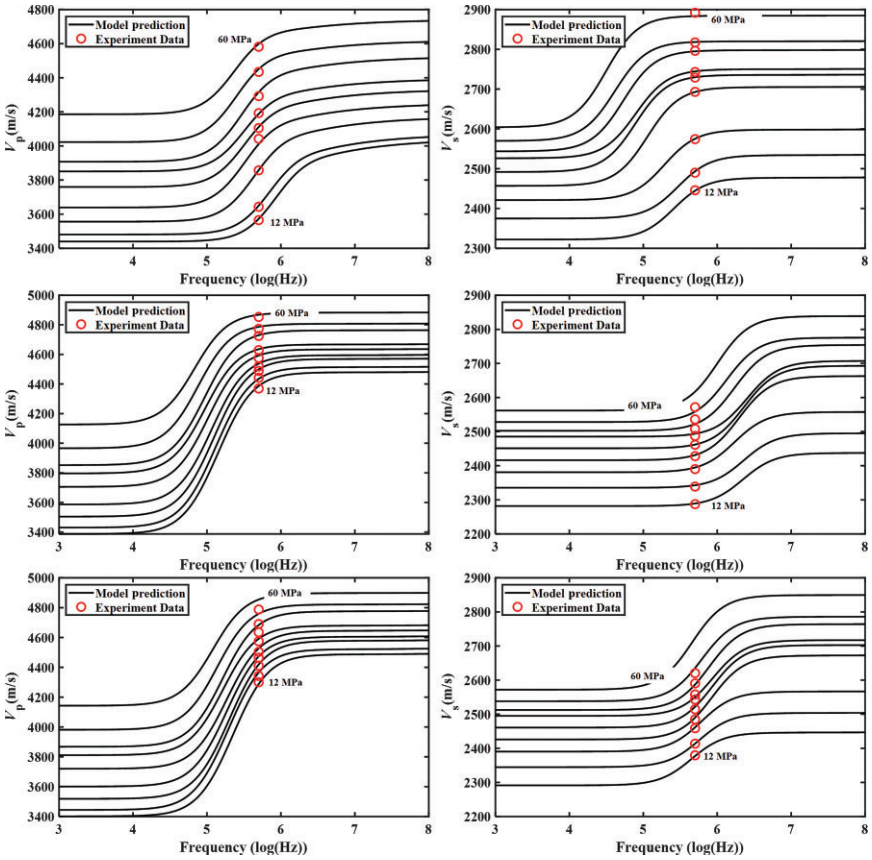

Figure 14 P-waves and S-waves velocities of sample TS1 under loading conditions and full saturations. (a) and (b) show the gas-saturated case; (c) and (d) show the water-saturated case; (e) and (f) show the oil-saturated case. The red circles represent experimental data.

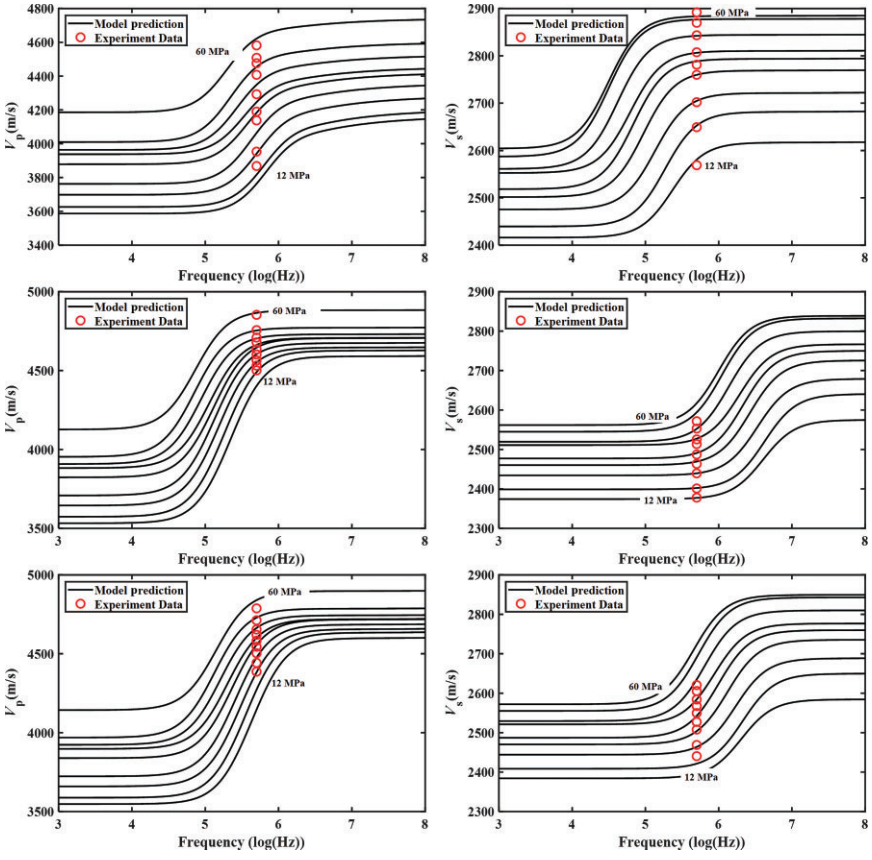

Figure 15 Same as Fig. 14 for unloading conditions.

observed at high pressures (see Fig. 12e and f), which may be attributed to the low porosity of the sample.

Conversely, Fig. 14 and Fig. 15 indicate that the wave velocities for the loading/unloading tests of TS1, respectively, compared with the data of experimental measurement. The results basically agree with the experimental data.

5. Conclusions

This study conducts the ultrasonic experiments on saturated tight sandstone samples under loading and unloading conditions. The inverse quality factors of P- and S-wave are calculated using the spectral ratio method.

The results indicate that with increasing pressure the wave velocities rise and attenuation declines. At a given pressure, the P-wave velocity is the highest for water-saturated conditions; conversely, the S-wave velocity follows the opposite trend. Attenuation is stronger for the water saturation case, followed by oil and gas saturation cases.

The velocity of P-wave and S-wave are lower in loading than those in unloading, and attenuation is higher in loading. This is attributed to the fact that the cracks cannot fully recover after unloading. A rock physics model is developed by using the VRH average, the DEM theory, and the squirt-flow model. The modeling indicates an agreement with the experimental measurement data, and provides a suitable characterization of the wave response of tight sandstones.

Additionally, the study illustrates the variation of pore structure parameters with pressure and fluid type. During loading, the soft porosity and aspect ratio decrease the most under gas saturation conditions and show the greatest change. After unloading, these properties are highest in the water-saturated case, followed by the oil-saturated case. Consequently, deformation is the lowest in the water-saturated case.

Acknowledgements

This work was funded by the National Natural Science Foundation of China (grant nos. 42104128 and 42174161) and the Natural Science Foundation of Jiangsu Province (grant no. BK20220995).

Conflict of interest statement

None declared.

Data availability

The data underlying this paper will be shared on reasonable request to the corresponding author.

References

Adam L, Batzle M, Lewallen K, Van Wijk K. 2009. Seismic wave attenuation in carbonates. *J Geophys Res Solid Earth*, **114**:B06208. https://doi.org/10.1029/2008JB005890

Ba J. 2013. *Progress and Review of Rock Physics*. Beijing: Tsinghua University Press.

Ba J, Xu W, Fu L, Carcione J, Zhang L. 2017. Rock anelasticity due to patchy saturation and fabric heterogeneity: a double double-porosity model of wave propagation. *J Geophys Res Solid Earth*, **122**:1949–76. https://doi.org/10.1002/2016JB013882

Ba J, Zhang L, Wang D, Yuan Z, Cheng W, Ma R, Wu C. 2018. Experimental analysis on P-wave attenuation in carbonate rocks and reservoir identification. *J Seism Explor*, **27**:371–402.

Ba J, Wei Y, Carcione J, Adam L, Tang G. 2024. Stress and frequency dependence of wave velocities in saturated rocks based on acoustoelasticity with squirt-flow dissipation. *Geophys J Int*, **236**:1753–63. https://doi.org/10.1093/gji/ggae020

Batzle M, Wang Z. 1992. Seismic properties of pore fluids. *Geophysics*, **57**:1396–524. https://doi.org/10.1190/1.1443207

Berryman J, Milton G. 1991. Exact results for generalized Gassmann equations in composite porous-media with two constituents. *Geophysics*, **56**:1930–2147. https://doi.org/10.1190/1.1443006

Berryman J. 2007. Seismic waves in rocks with fluids and fractures. *Geophys J Int*, **171**:954–74. https://doi.org/10.1111/j.1365-246X.2007.03563.x

Biot M. 1956. Theory of propagation of elastic waves in fluid-saturated porous solid. I. Low-frequency range. *J Acoust Soc Am*, **28**:168–78. https://doi.org/10.1121/1.1908239

Biot M. 1962. Mechanics of deformation and acoustic propagation in porous media. *J Appl Phys*, **33**:1482–98. https://doi.org/10.1063/1.1728759

Bourbié T, Coussy O, Zinszner B. 1987. *Acoustics of Porous Media*. Paris: Editions Technip.

Carcione J, Morency C, Santos J. 2010. Computational poroelasticity—a review. *Geophysics*, **75**:A229–43. https://doi.org/10.1190/1.3474602

Carcione J. 2022. *Wave Fields in Real Media: Theory and Numerical Simulation of Wave Propagation in Anisotropic, Anelastic, Porous and Electromagnetic Media*, 4th edn. Amsterdam: Elsevier.

Chapman M. 2003. Frequency dependent anisotropy due to mesoscale fractures in the presence of equant porosity. *Geophys Prospect*, **51**:369–79. https://doi.org/10.1046/j.1365-2478.2003.00384.x

Chapman S, Tisato N, Quintal B, Holliger K. 2016. Seismic attenuation in partially saturated Berea sandstone submitted to a range of confining pressures. *J Geophys Res Solid Earth*, **121**:1664–76. https://doi.org/10.1002/2015JB012575

Chen F, Zong Z, Yin X, Yang Z, Yan X. 2023. Pressure and frequency dependence of elastic moduli of fluid-saturated dual-porosity rocks. *Geophys Prospect*, **71**:1599–615. https://doi.org/10.1111/1365-2478.13395

Chen F, Zong Z, Yin Y. 2025. A squirt-flow model in isotropic porous rocks containing wedge-shaped cracks and its interpretation for laboratory measurements. *Geophysics*, **90**:MR141–53. https://doi.org/10.1190/geo2024-0292.1

David E, Fortin J, Schubnel A. 2013. Laboratory measurements of low- and high-frequency elastic moduli in Fontainebleau sandstone. *Geophysics*, **78**:D369–79. https://doi.org/10.1190/geo2013-0070.1

Dvorkin J, Nur A. 1993. Dynamic poroelasticity: a unified model with the squirt and the Biot mechanisms. *Geophysics*, **58**:466–599. https://doi.org/10.1190/1.1443435

Dvorkin J, Nolen-Hoeksema R, Nur A. 1994. The squirt-flow mechanism: macroscopic description. *Geophysics*, **59**:336–490. https://doi.org/10.1190/1.1443605

Gardner G, Wyllie M, Droschak D. 1964. Effects of pressure and fluid saturation on the attenuation of elastic waves in sands. *J Pet Technol*, **16**:189–98. https://doi.org/10.2118/721-PA

Gassmann F. 1951. Über die Elastizität poröser Medien: vierteljahrsschrift der. *Naturforschenden Gesellschaft in Zürich*, **96**: 1–23.

Gurevich B, Makarynska D, Paula O, Pervukhina M. 2010. A simple model for squirt-flow dispersion and attenuation in fluid-saturated granular rocks. *Geophysics*, **75**:N109–20. https://doi.org/10.1190/1.3509782

Han T, Liu B, Sun J. 2018. Validating the theoretical model for squirt-flow attenuation in fluid saturated porous rocks based on the dual porosity concept. *Geophys J Int*, **214**:1800–07. https://doi.org/10.1093/gji/ggy241

Hill R. 1952. The elastic behaviour of a crystalline aggregate. *Proc Phys Soc*, **65**:349–54. https://doi.org/10.1088/0370-1298/65/5/307

Johnston D, Toksöz N, Timur A. 1979. Attenuation of seismic waves in dry and saturated rocks: II. *Mechanisms. Geophysics*, **44**:691–711. https://doi.org/10.1190/1.1440970

Johnston D, Toksöz M. 1980. Ultrasonic P and S wave attenuation in dry and saturated rocks under pressure. *J Geophys Res Solid Earth*, **85**:925–36. https://doi.org/10.1029/JB085iB02p00925

King M. 2005. Rock-physics developments in seismic exploration: a personal 50-year perspective. *Geophysics*, **70**:1ND–Z113. https://doi.org/10.1190/1.2107947

Ma R, Ba J, Carcione J, Zhou X, Li F. 2019. Dispersion and attenuation of compressional waves in tight oil reservoirs: experiments and simulations. *Appl Geophys*, **16**:33–45. https://doi.org/10.1007/s11770-019-0748-3

Ma R, Ba J. 2020. Coda and intrinsic attenuation from ultrasonic measurements in tight siltstones. *J Geophys Res Solid Earth*, **125**:e2019JB018825. https://doi.org/10.1029/2019JB018825

Mavko G, Jizba D. 1991. Estimating grain-scale fluid effects on velocity dispersion in rocks. *Geophysics*, **56**:1940–49. https://doi.org/10.1190/1.1443005

Müller T, Gurevich B, Lebedev M. 2010. Seismic wave attenuation and dispersion resulting from wave-induced flow in porous rocks—a review. *Geophysics*, **75**:A147–64. https://doi.org/10.1190/1.3463417

Oh T, Kwon T, Cho G. 2011. Effect of partial water saturation on attenuation characteristics of low porosity rocks. *Rock Mech Rock Eng*, **44**:245–51. https://doi.org/10.1007/s00603-010-0121-6

Pan X, Ba J, Ma R, Liu W, Cheng W, Carcione J. 2023. Effects of pressure and fluid properties on S-wave attenuation of tight rocks based on ultrasonic experiments. *Appl Geophys*, **21**: 246–64. https://doi.org/10.1007/s11770-024-1053-3

Picotti S, Carcione J. 2006. Estimating seismic attenuation (Q) in the presence of random noise. *J Seism Explor*, **15**:165–81.

Quan Y, Harris J. 1997. Seismic attenuation tomography using the frequency shift method. *Geophysics*, **62**:895–905. https://doi.org/10.1190/1.1444197

Reuss A. 1929. Berechnung der fliessgrenze von mischkristallen auf grund der plastizitatsbedingungen fur einkristalle. *Zeitschrift fur Angewandte Mathematic und Mechanik*, **9**:49–58. https://doi.org/10.1002/zamm.19290090104

Sams M, Neep J, Worthington M, King M. 1997. The measurement of velocity dispersion and frequency-dependent intrinsic attenuation in sedimentary rocks. *Geophysics*, **62**:1456–64. https://doi.org/10.1190/1.1444249

Tao G, King M, Nabi-Bidhendi M. 1995. Ultrasonic wave propagation in dry and brine-saturated sandstones as a function of effective stress: laboratory measurements and modelling. *Geophys Prospect*, **43**:299–327. https://doi.org/10.1111/j.1365-2478.1995.tb00255.x

Toksöz M, Johnston D, Timur A. 1979. Attenuation of seismic waves in dry and saturated rocks: I. Laboratory measurements. *Geophysics*, **44**:681–90. https://doi.org/10.1190/1.1440969

Wang D, Xin K, Li M, Gao J, Wu X. 2006. An experimental study of influence of water saturation on velocity and attenuation in sandstone under stratum conditions. *Chin J Geophys*, **49**:908–14.

White J. 1975. Computed seismic speeds and attenuation in rocks with partial gas saturation. *Geophysics*, **40**:224–32. https://doi.org/10.1190/1.9781560802471

Winkler K, Nur A. 1979. Pore fluids and seismic attenuation in rocks. *Geophys Res Lett*, **6**:1–4. https://doi.org/10.1029/GL006i001p00001

Zhang C, Ulrych T. 2002. Estimation of quality factors from CMP records. *Geophysics*, **67**:1542–47. https://doi.org/10.1190/1.1512799

Zhang L, Ba J, Yin W, Sun W, Tang J. 2017. Seismic wave propagation equations of conglomerate reservoirs: a triple-porosity structure model. *Chin J Geophys (in Chinese)*, **60**:1073–87. https://doi.org/10.6038/cjg20170329

Zhu H, Ba J, Zhang L, Carcione J, Yan X. 2024. Effect of temperature and fluid on rock microstructure based on an effective medium theory. *J Geophys Eng*, **21**:426–37. https://doi.org/10.1093/jge/gxae014

Zhu X, Pan R, Zhu S, Wei W, Ye L. 2018. Research progress and core issues in tight reservoir exploration. *Earth Sci Front*, **25**:141–46. https://doi.org/10.13745/j.esf.2018.02.015

Zhubayev A, Houben M, Smeulders D, Barnhoorn A. 2016. Ultrasonic velocity and attenuation anisotropy of shales, Whitby, United Kingdom. *Geophysics*, **81**:D45–56. https://doi.org/10.1190/geo2015-0211.1

Zou C, Zhang G, Yang Z. 2013. Concepts, characteristics, potential and technology of unconventional hydrocarbons: on unconventional petroleum geology. *Pet Explor Dev Online*, **40**:413–28. https://doi.org/10.1016/S1876-3804(13)60053-1

Zou C, Yang Z, Zhang G. 2019. Establishment and practice of unconventional oil and gas geology. *Acta Geol Sin*, **93**:12–23. https://doi.org/10.19762/j.cnki.dizhixuebao.2019002

Zou C, Qiu Z. 2021. Preface: New advances in unconventional petroleum sedimentology in China. *Acta Sedimentol Sinica*, **39**:1–9. https://doi.org/10.14027/j.issn.1000-0550.2021.001

Received: 23 March 2025. **Revised:** 13 May 2025. **Accepted:** 9 June 2025